Detection, Attribution, and Projection of Regional Rainfall Changes on (Multi-) Decadal Time Scales: A Focus on Southeastern South America

Honghai Zhang

Program in Atmospheric and Oceanic Sciences, Princeton University, and NOAA/Geophysical Fluid Dynamics Laboratory, Princeton, New Jersey

Thomas L. Delworth, Fanrong Zeng, Gabriel Vecchi, and Karen Paffendorf

NOAA/Geophysical Fluid Dynamics Laboratory, Princeton, New Jersey

Liwei Jia

Program in Atmospheric and Oceanic Sciences, Princeton University, and NOAA/Geophysical Fluid Dynamics Laboratory, Princeton, New Jersey

(Manuscript received 7 April 2016, in final form 22 August 2016)

ABSTRACT

Observed austral summertime (November through April) rainfall in southeastern South America (SESA)—including northern Argentina, Uruguay, southern Brazil, and Paraguay—has exhibited substantial low-frequency variations with a multidecadal moistening trend during the twentieth century and a subsequent decadal drying trend during the current century. Understanding the mechanisms responsible for these variations is essential for predicting long-term rainfall changes. Here with a suite of attribution experiments using a pair of high-resolution global climate models, GFDL CM2.5 and FLOR-FA, the authors investigate the causes of these regional rainfall variations. Both models reproduce the twentieth-century moistening trend, albeit with a weaker magnitude than observed, in response to the radiative forcing associated with increasing greenhouse gases. The increasing greenhouse gases drive tropical expansion; consequently, the subtropical dry branch of Hadley cell moves away from SESA, leading to the rainfall increase. The amplitude discrepancy between the observed and simulated rainfall changes suggests a possible underestimation by the models of the atmospheric response to the radiative forcing, as well as an important role for low-frequency internal variability in the observed moistening trend. Over the current century, increasing greenhouse gases drive a continuous SESA rainfall increase in the models. However, the observed decadal rainfall decline is largely (~60%) reproduced in response to the observed Pacific trade wind strengthening, which is likely associated with natural Pacific decadal variability. These results suggest that the recent summertime rainfall decline in SESA is temporary and that the positive trend will resume in response to both increasing greenhouse gases and a return of Pacific trade winds to normal conditions.

1. Introduction

The summertime (November through April) rainfall in southeastern South America (SESA), defined here as the region 40°–25°S, 65°–45°W, has experienced substantial interannual-to-multidecadal changes during the past century (precipitation time series in Fig. 1 and map of region in Fig. 2). These observed low-frequency changes have imposed profound impacts on regional agriculture development and water resource management (e.g., Robertson and Mechoso 1998; Viglizzo and Frank 2006), inspiring many efforts to understand the underlying physical processes and to predict future changes. On interannual time scales, the rainfall changes in SESA have received substantial investigation [see Seager et al. (2010) for a review, and the references therein], but on decadal-to-multidecadal time scales there are fewer studies on this topic and there is still much debate about the associated physical mechanisms (e.g., Huang et al. 2005; Seager et al. 2010; Gonzalez et al. 2014).

On decadal and longer time scales, observed changes of summertime rainfall in SESA are characterized by two distinctive trends: a multidecadal positive trend
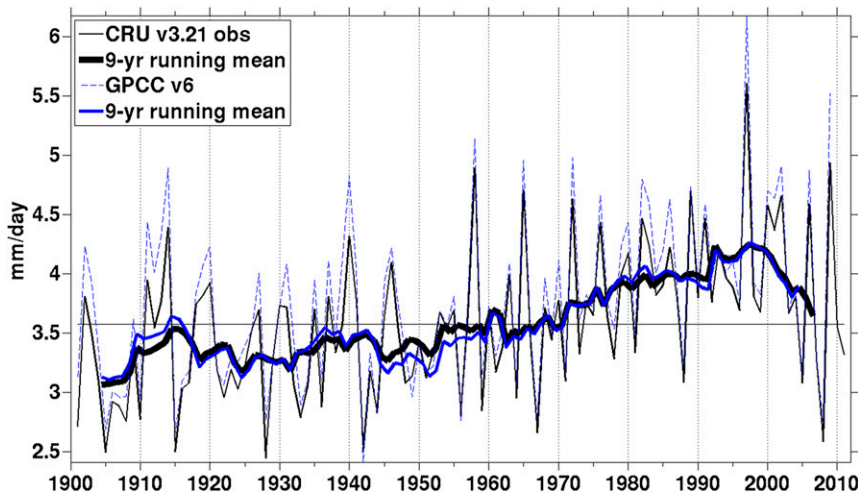

FIG. 1. Observed monthly mean (thin curves) and 9-yr running mean (thick curves) precipitation time series averaged over SESA (40°–25°S, 65°–45°W) during austral summer (NDJFMA) from CRU (black) and GPCC (blue) data. The monthly mean time series has a long-term mean of 3.58 mm day^{-1} for CRU and 3.77 mm day^{-1} for GPCC data. In order for a direct comparison of the decadal-to-multidecadal variability between the two datasets, the GPCC 9-yr running mean series (not the monthly series) has been adjusted to share the same long-term mean as the CRU series. The 9-yr running mean series has a standard deviation of 0.31 mm day^{-1} for CRU and 0.32 mm day^{-1} for GPCC data. The linear trend of the CRU monthly time series is about 0.06 mm day^{-1} decade^{-1} during 1901–70 and 0.18 mm day^{-1} decade^{-1} during 1970–2000.

over the twentieth century, with a larger rate in the second half of the century than in the first half, and a decadal negative trend starting around the turn of the century (Fig. 1). The multidecadal positive trend has been suggested to arise from two different physical sources—internal climate variability and external radiative forcing. On one hand, Seager et al. (2010) argued that multidecadal variations of the SESA precipitation are mainly driven by the Atlantic multidecadal oscillation (AMO). Specifically, in an atmospheric general circulation model (AGCM) the cold sea surface temperature (SST) anomalies in the tropical Atlantic associated with a cold phase of the AMO drive upper-tropospheric equatorward flow southwest of the tropical heating anomalies (Gill-type response; Gill 1980), which then via vorticity advection induces anomalous vortex stretching and ascent and thus increased rainfall over SESA. A new study by Ruprich-Robert et al. (2016, manuscript submitted to *J. Climate*) examines the global climate response to the AMO in two different global climate models and presents similar evidence for a moistening response in SESA to a negative phase of the AMO. On the other hand, external radiative forcing has also been suggested to play a role in the observed twentieth-century moistening trend over SESA (e.g., Jones and Carvalho 2013). In particular, ozone depletion over the high latitudes of the Southern

Hemisphere has been proposed to be the main cause of the SESA wetting trend during the late twentieth century (Kang et al. 2011; Gonzalez et al. 2014). Using two different climate models, Kang et al. (2011) found that the poleward shift of the Southern Hemisphere extratropical jet induced by prescribed ozone depletion leads to a general moistening trend during austral summer in the southern subtropics. This extratropics–tropics linkage, although only strictly applicable in the zonal mean sense, is then employed by Gonzalez et al. (2014) to interpret the observed summertime precipitation increase over SESA via comparing simulations with and without ozone depletion from multiple climate models. However, owing to the weak and inconsistent rainfall response among the models used in Gonzalez et al. (2014; see Figs. 4, 6, 7, and 8 therein), there is some uncertainty in the role of ozone depletion; in addition, their results also suggest some role for increasing greenhouse gases, further confounding the causes of the multidecadal summertime moistening trend in SESA during the late twentieth century.

Complicating the interpretation of the twentieth-century multidecadal SESA summertime moistening is the recent decadal rainfall decline starting around the beginning of the current century (Fig. 1). Although the specific reasons for this decadal decline are yet to be explored, insights can be gained from previous studies on
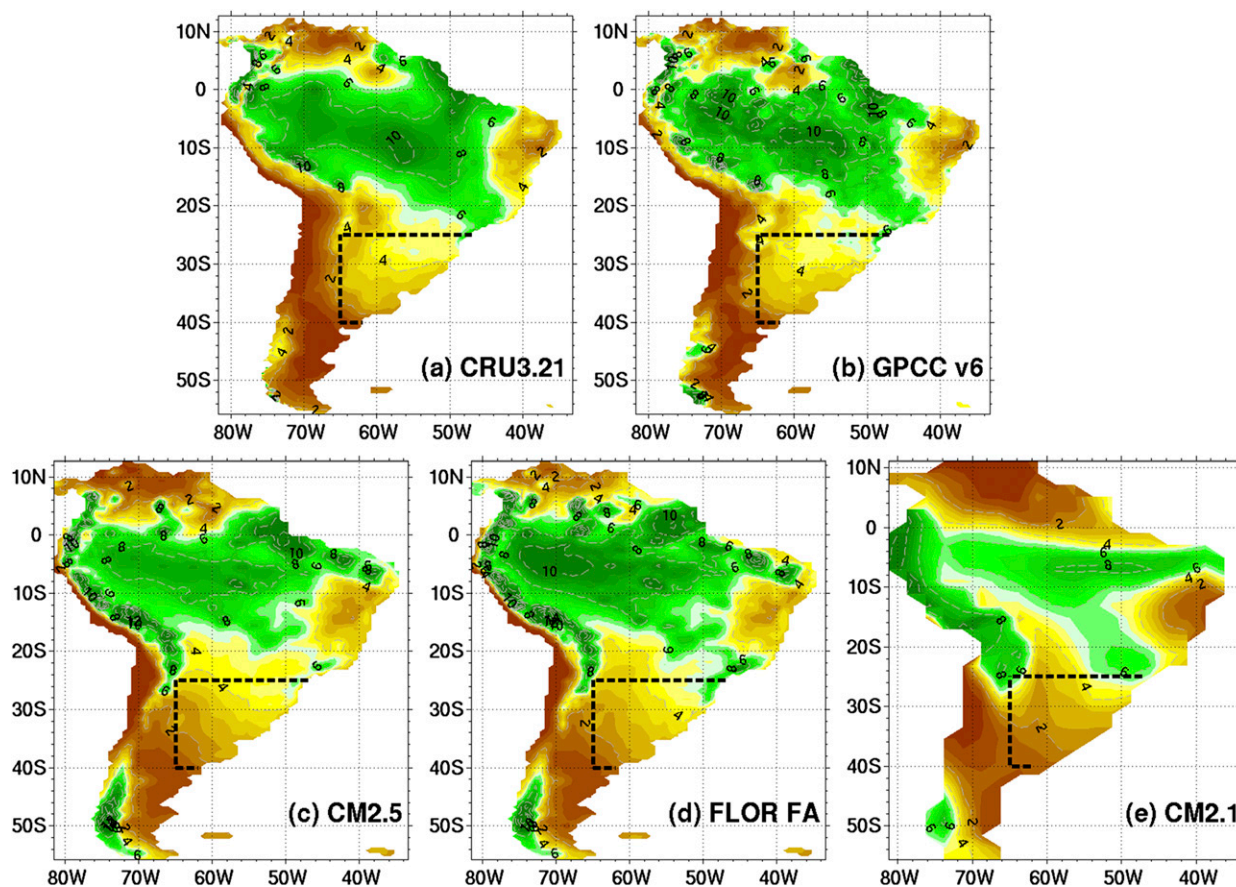
FIG. 2. Climatological precipitation (mm day^{-1}) during 1901–2010 for austral summer (NDJFMA) in (a) CRU and (b) GPCC observations and (c) CM2.5, (d) FLOR-FA, and (e) CM2.1 historical simulations. The black-dashed areas indicate the SESA region where the precipitation time series in Fig. 1 is averaged. A more quantitative comparison between observations and models is listed in Table 1.

decadal variations of summertime rainfall in SESA. On decadal time scales, Pacific decadal variability (PDV) has been shown to play a crucial role in the observed precipitation changes across South America. Huang et al. (2005) investigated precipitation changes associated with the 1976/77 climate shift over the Americas with an atmospheric general circulation model, and found that the anomalous warm state of the tropical Pacific during the two decades following the climate shift contributes to the observed rainfall increase over central South America including the SESA region. Based on simulations from phase 5 of the Coupled Model Intercomparison Project (CMIP5), Boisier et al. (2016) attributed about 50% of the observed rainfall decline in central Chile since the late 1970s to the concurrent positive-to-negative phase transition of the PDV. In both studies, changes in the tropical Pacific associated with the PDV impact precipitation variability across South America via modifying large-scale atmospheric circulation. These results imply that the PDV may play a role in the recent summertime rainfall decline in SESA.

Understanding the observed decadal-to-multidecadal rainfall variations in SESA will help to predict long-term changes that are important for the development of regional agriculture and management of water resources in the coming decades. Here we focus on the two distinctive trends of the observed summertime rainfall changes in SESA—the multidecadal increase during the twentieth century and the recent decadal decline—and investigate the underlying mechanisms with a modeling approach. We make use of two comprehensive suites of simulations performed with high-resolution global climate models developed at the Geophysical Fluid Dynamics Laboratory (GFDL). These simulations have previously been used to investigate causes of observed regional rainfall decline in southwestern Australia (Delworth and Zeng 2014), observed rainfall changes in western North America (Delworth et al. 2015), and observed changes in extratropical storminess (Yang et al. 2015) and heat waves (Jia et al. 2015) over North America. The suites include 1) historical simulations aimed to assess the climate response to observed

estimates of changes in atmospheric composition dating back to the late nineteenth century, 2) attribution simulations to determine the specific impacts of different types of radiative forcing agents, and 3) simulations of future climate using projected changes in radiative forcing.

2. Data and model simulations

a. Observations

The precipitation data used here are from the Climatic Research Unit (CRU) at the University of East Anglia, version 3.21 (v3.21). This dataset, constructed from observations at meteorological stations, provides monthly gridded land rainfall time series at 0.5° resolution for the period of 1901–2012 (Harris et al. 2014). We also use the Global Precipitation Climatology Centre (GPCC),[1] version 6 (v6), dataset at 0.5° resolution from 1901 to 2010 (Schneider et al. 2011). The quality of these gridded precipitation products in SESA—particularly in terms of the long-term trend and low-frequency variability—has been examined by Gonzalez et al. (2013) and shown to be consistent with station-based observations. In SESA during austral summer [defined as the period from November to April (NDJFMA)], the two datasets show slightly different climatologies with a long-term mean of 3.58 mm day^{-1} for CRU versus 3.77 mm day^{-1} for GPCC data (Fig. 1). This discrepancy is due to the fact that they are constructed by adding observed monthly precipitation anomalies to two different existing climatologies (Harris et al. 2014; Schneider et al. 2011). On the decadal-to-multidecadal time scales of interest here, the precipitation variability in the two datasets is very similar (Fig. 1). With a standard deviation of 0.31 mm day^{-1} for CRU and 0.32 mm day^{-1} for GPCC data and a correlation coefficient of 0.97 between them, both precipitation series (9-yr running mean) capture the multidecadal positive trend of varying rates during the last century and the recent decadal decline during the current century. In the following, we only present results from the CRU dataset.

b. Model simulations

In this study we use two climate models: the GFDL Climate Model version 2.5 (CM2.5) (Delworth et al. 2012) and its variant, the flux-adjusted version of the Forecast-Oriented Low Ocean Resolution (FLOR-FA)

model (Vecchi et al. 2014). Compared to its widely used predecessor CM2.1 (Delworth et al. 2006), CM2.5 is developed with specific efforts in refining the spatial resolution. The atmospheric component of CM2.5 has a horizontal resolution of approximately 50 km and 32 vertical levels, in contrast to the roughly 200-km horizontal grid spacing and 24 vertical levels in CM2.1; the horizontal resolution of the oceanic component has increased from about 100 km in CM2.1 to a much finer grid varying from 28 km at the equator to 8 km at high latitudes in CM2.5 (the 50-level vertical resolution remains the same). With the refined spatial resolution, CM2.5 has improved many aspects of the simulated mean climate state and climate variability on various spatial and temporal scales (see Delworth et al. 2012). Of particular interest for this study is the improvement in the simulation of regional precipitation. Over South America, the refined spatial resolution in CM2.5 has brought the simulated climatological summertime (NDJFMA) precipitation much closer to observations than in CM2.1 (Fig. 2 and Table 1): the spatial pattern correlates with CRU observations at 0.71 in CM2.5 versus 0.45 in CM2.1; the amplitude of the area-averaged precipitation— 5.09 mm day^{-1} in CRU observations—is 5.05 mm day^{-1} in CM2.5 versus 4.28 mm day^{-1} in CM2.1, with a root-mean-square error of 2.22 mm day^{-1} in CM2.5 versus 3.00 mm day^{-1} in CM2.1 (similar results are obtained using GPCC; see Table 1). The improvement in the simulation of regional precipitation increases our confidence in investigating the physical mechanisms of decadal-to-multidecadal changes of summertime rainfall in SESA in CM2.5.

FLOR-FA couples the low-resolution ocean and sea ice components of CM2.1 with the high-resolution atmosphere and land components of CM2.5. Flux adjustments are implemented upon the atmosphere-to-ocean fluxes of enthalpy, freshwater, and momentum to reduce the model biases in the long-term climatology of sea surface temperature, salinity, and surface wind stress fields. Consequently, the climatology of other fields and the atmospheric teleconnections have also been improved in FLOR-FA (Vecchi et al. 2014; Jia et al. 2015). Relative to CM2.5, the FLOR-FA version substantially lowers the computational cost, but still retains the improvements in the simulation of regional climate achieved in CM2.5 relative to CM2.1 due to using both the same atmosphere and land components and the flux adjustment (see Fig. 2 and Table 1) (e.g., Vecchi et al. 2014).

Two suites of simulations—performed with CM2.5 and FLOR-FA, respectively—are analyzed to investigate the decadal-to-multidecadal rainfall changes across South America with a focus on SESA (Table 2).

---

[1] The GPCC precipitation data are provided by the NOAA/OAR/ESRL Physical Sciences Division (PSD), Boulder, Colorado, from their website at http://www.esrl.noaa.gov/psd/data/gridded/data.gpcc.html.

TABLE 1. Comparison of the summertime (NDJFMA) climatological (1901–2010) precipitation over South America (56°S–13°N, 82°–33°W) among CRU and GPCC observations and model simulations (see Fig. 2). For the comparison between observations and models, the RMSE and correlation values indicate the comparison between CRU (GPCC in parentheses) data and models; while for the comparison between the two observations, CRU data is taken as the reference (and thus has a RMSE of 0 mm day^{-1} and a spatial correlation coefficient of 1).

	Areal mean (mm day^{-1})	RMSE (mm day^{-1})	Spatial correlation
CRU v3.21	5.08	0	1
GPCC v6	5.20	1.02	0.94
CM2.1	4.28	3.00 (3.07)	0.45 (0.46)
CM2.5	5.04	2.22 (2.19)	0.71 (0.73)
FLOR-FA	5.64	2.43 (2.38)	0.71 (0.72)

The CM2.5 simulations are the primary dataset used to attribute the twentieth-century multidecadal rainfall increase in SESA. In this suite, a 1100-yr control simulation (CNTL) is conducted in which the concentration of atmospheric greenhouse gases and aerosols is kept at a constant value that is representative of preindustrial conditions (corresponding approximately to calendar year 1860). This simulation serves as a reference and provides a set of initial conditions for all other forced simulations. A five-member ensemble of historical simulations (ALLFORC), initialized from different times of CNTL (years 101, 141, 181, 221, and 261), is driven by observed estimates of changes in atmospheric composition (including greenhouse gases, ozone, aerosols with direct effect only), land use, volcanic aerosols, and solar irradiance from 1861 to 2005 and extended further to 2100 with estimated forcing corresponding to the representative concentration pathway 8.5 (RCP8.5) scenario from the Intergovernmental Panel on Climate Change (IPCC) protocols (Meinshausen et al. 2011). Five three-member ensemble simulations, to attribute the external causes of climate changes simulated in ALLFORC, are driven by different subsets of total forcing: anthropogenic activity (ANTHRO), natural processes (NATURAL, volcanic aerosols and solar irradiance), well-mixed greenhouse gases (GHG), ozone in both troposphere and stratosphere (OZONE), and anthropogenic aerosols (AEROSOL, direct effect only). The three members of these ensembles are initialized from CNTL at years 101, 141, and 181, the same as the first three members of ALLFORC. These three ALLFORC members will be used in the case of comparison with the attribution simulations.

To further quantify the relative roles of external forcing (ensemble mean) versus internal variability (ensemble spread) in the twentieth-century multidecadal summertime rainfall increase in SESA, we analyze a complementary dataset including two large ensembles performed with FLOR-FA. The first ensemble includes 35 historical simulations, with 5 long members integrating from 1861 to 2100 and 30 short

members extending from 1941 to 2050, using the same twentieth-century forcing as CM2.5 ALLFORC but using the representative concentration pathway 4.5 (RCP4.5) emission scenario after 2006 (with the same constant flux adjustment as before 2006). This set of experiments is referred to as FLOR-FA ALLFORC. The 5 long simulations (1861–2100) are initialized from years 101, 141, 181, 221, and 261 of a 3500-yr FLOR-FA control run (FLOR-FA CNTL, the same preindustrial forcing as in CM2.5 CNTL). The 30 shorter simulations (1941–2050) are initialized from the 5 long simulations as follows: the first (second and third) 10 simulations share the same ocean initial conditions that are taken from year 1941 of the first (second and third) long simulation but have different atmosphere–land initial conditions that are taken from years 1940 and 1942 of the 5 long simulations, respectively. The second large ensemble has 30 simulations that are identical to the 30 short 1941–2050 historical simulations except that their forcing only includes the natural processes (solar irradiance and volcanic aerosols, as in CM2.5 NATURAL) and the atmospheric composition is held at 1941 conditions (FLOR-FA NATURAL). The differences between the two large ensembles (FLOR-FA ALLFORC and FLOR-FA NATURAL) thus reflect the impacts of anthropogenic forcing. Despite the relatively short simulation length (starting in 1941 as opposed to in 1861 in the CM2.5 suite), these two large ensembles provide more realizations of internal variability in the coupled climate system, and thus are very useful in attributing the potential sources of the twentieth-century multidecadal rainfall changes.

To investigate the recent decadal rainfall decline in SESA and particularly the potential role of the Pacific decadal variability, we analyze another suite of simulations that is specifically designed by Delworth et al. (2015) to assess the impact of the observed Pacific decadal variability on global climate. Performed with FLOR-FA, this suite includes the 35-member ensemble of historical simulations (FLOR-FA ALLFORC) and a 35-member ensemble of sensitivity simulations that only

TABLE 2. CM2.5 and FLOR-FA simulations.

Expt name	No, of ensemble members	Period of simulation (years)	Radiative forcing
CM2.5			
CNTL	1	1–1100	Atmospheric composition fixed at preindustrial level (1860), no volcanic eruptions or solar irradiance changes.
ALLFORC	5	1861–2100	Observational estimates of changes in greenhouse gases, anthropogenic aerosols (only direct effect), ozone, land use, solar irradiance and volcanic eruptions for 1861–2005; for the period after 2005, the IPCC RCP8.5 forcing scenario is used.
ANTHRO	3	1861–2012	The same as ALLFORC, except uses constant 1860 solar irradiance and no volcanic eruptions.
NATURAL	3	1861–2012	For 1861–2005, observational estimates of changes in solar irradiance and volcanic eruptions, with atmospheric composition fixed at 1860 conditions; for 2006–12, an estimated solar cycle is used, with no volcanic eruptions.
GHG	3	1861–2012	For 1861–2005, observational estimates of changes in well-mixed greenhouse gases; for 2006–12, estimates from IPCC RCP8.5 scenario are used; all other forcing held at 1860 level.
OZONE	3	1861–2012	For 1861–2005, observational estimates of changes in tropospheric and stratospheric ozone; for 2006–12, estimates from IPCC RCP8.5 scenario are used; all other forcing held at 1860 level.
AEROSOL	3	1861–2012	For 1861–2005, observational estimates of changes in anthropogenic aerosols (only direct effect); for 2006–12, estimated anthropogenic aerosols from IPCC RCP8.5 scenario are used; all other forcing held at 1860 level.
FLOR-FA			
CNTL	1	1–3500	Atmospheric composition fixed at preindustrial level (1860), no volcanic eruptions or solar irradiance changes.
ALLFORC	35	1861–2100 (5 members) 1941–2050 (30 members)	Observational estimates of changes in greenhouse gases, anthropogenic aerosols (only direct effect), ozone, land use, solar irradiance and volcanic eruptions for 1861 (1941)–2005; for the period after 2005, the IPCC RCP4.5 forcing scenario is used.
ALLFORC_STRESS	35	1979–2013	The same as ALLFORC, except that the model-computed wind stress monthly anomalies are replaced with observation-based wind stress monthly anomalies for 1979–2013.
NATURAL	30	1941–2050	For 1941–2005, observational estimates of changes in solar irradiance and volcanic aerosols, with atmospheric composition held at the constant 1941 conditions; for 2006–50, an estimated solar cycle is used, with no volcanic eruptions.

differ from the historical simulations by the wind stress configuration in the tropical Pacific (ALLFORC_STRESS). In ALLFORC, the wind stress is computed by the model itself on the basis of its transient atmosphere and ocean states, while in ALLFORC_STRESS, the model-computed wind stress anomalies in the tropical Pacific (25°N–25°S) are overridden by the observation-based wind stress anomalies for the period of 1979–2013. The prescribed wind stress anomalies are derived from the European Centre for Medium-Range Weather Forecasts (ECMWF) interim reanalysis (ERA-Interim). The overriding in the tropical Pacific only affects the momentum flux into the ocean and is applied on a month by month basis; that is, the model-computed monthly anomalies are replaced with the observation-based monthly anomalies, while the climatological seasonal cycle is unaltered [refer to Delworth et al. (2015) for more details on the experiment implementation]. The difference between ALLFORC and ALLFORC_STRESS represents the impacts on the global climate system of the changes in the observed monthly momentum flux into the tropical Pacific during 1979–2013.

3. Results

a. Multidecadal positive precipitation trend during the twentieth century

The observed summertime (NDJFMA) precipitation over SESA shows a multidecadal positive trend of varying rate during the twentieth century. In particular, the period prior to 1960 is drier than the long-term average, whereas the period after 1970 is wetter (Fig. 1). To investigate this centennial moistening trend, we will focus on the difference in the mean climate state between two periods: the drier 1901–50 period and the wetter 1981–2010 period (note that choosing slightly different periods, for instance, 1901–70 and/or 1981–2000, does not change the conclusions presented below). Figure 3a illustrates the observed mean NDJFMA precipitation difference (the latter period minus the earlier period) in South America. As expected, the SESA region shows a wetter condition in the late twentieth century relative to the earlier period, and the difference is significant at the 5% significance level based on a two-sided Student's t test.[2] To the north and southwest of

---

[2] Here we test the null hypothesis that the seasonal precipitation time series during the two periods are independent random samples with equal means against the alternative hypothesis that the means are not equal. Under the null hypothesis, the test parameter, $t = (\bar{x} - \bar{y})/\sqrt{v_x/m + v_y/n}$ with bars indicating the sample means, v the sample variance, and m and n the sample sizes, has a Student's t distribution with $m + n - 2$ degrees of freedom.
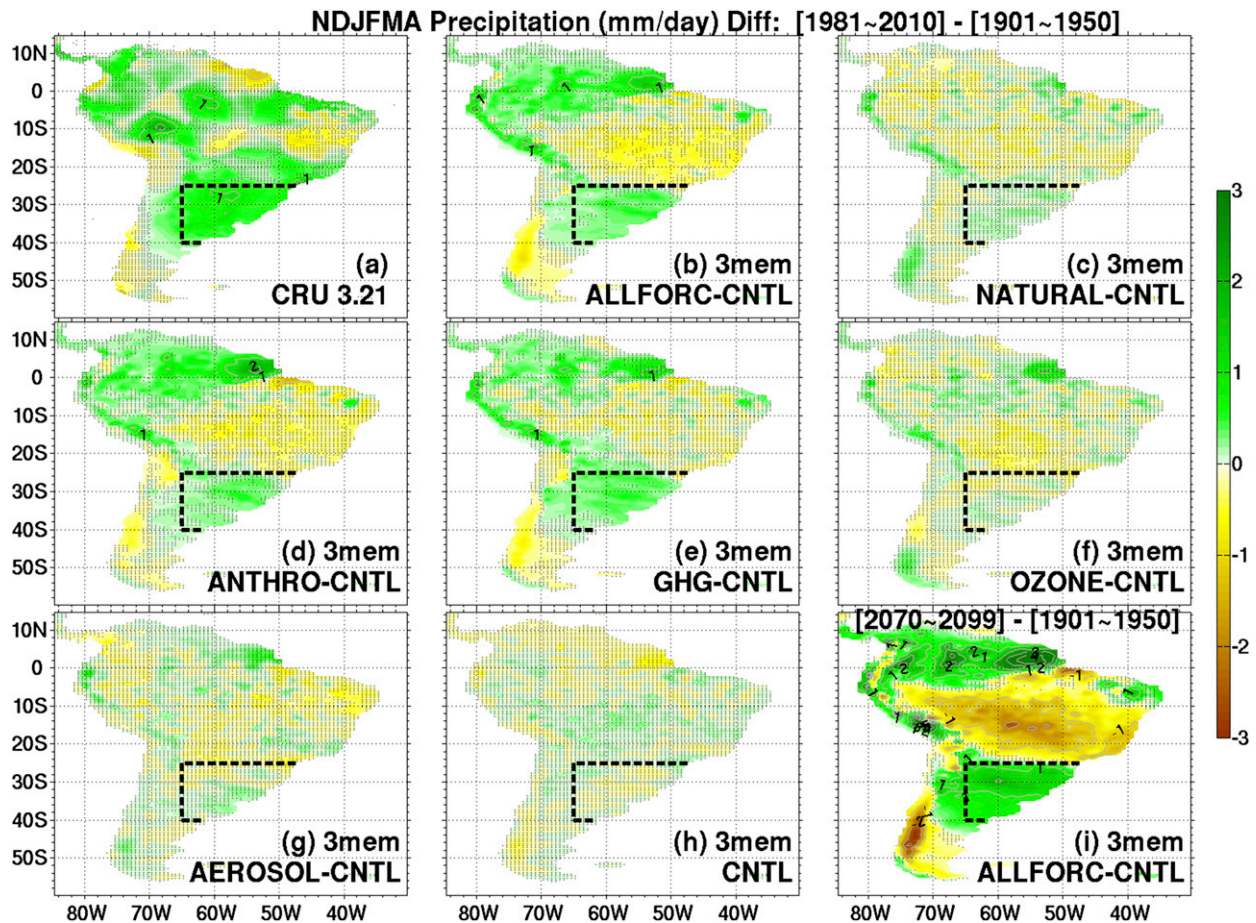
SESA are weak and insignificant drier conditions, except for some scattered significant wetter conditions to the north.

How well is the observed precipitation change in South America simulated in CM2.5? North of about 20°S, the three-member ensemble mean (similar results for five members) of the historical simulations (ALLFORC) bears a somewhat coherent pattern of central South American drying (0°–20°S) and equatorial South American moistening (Fig. 3b), inconsistent with the observed precipitation change of scattered drying and wetting. However, the lack of observations during the twentieth century in the Amazon makes it difficult to evaluate the model's performance in this region. South of about 20°S where gridded rainfall products (e.g., CRU and GPCC) are in good agreement with station-based observations (Gonzalez et al. 2013), ALLFORC reproduces the spatial pattern of the observed precipitation changes, including the moistening in SESA and the drying southwest of SESA (cf. Figs. 3a and 3b). The simulated precipitation increase in SESA, albeit with a smaller amplitude than observations (see more discussion below), passes the 5% significance test. In contrast to ALLFORC, the control simulations (CNTL, Fig. 3h; differencing the two periods of CNTL corresponding to the calendar periods of ALLFORC) on which ALLFORC is based fail in replicating these observed precipitation changes, suggesting a substantial role for the transient radiative forcing in driving the summertime positive precipitation trend in SESA.

1) ROLE OF EXTERNAL RADIATIVE FORCING

The "externally forced" summertime moistening signal in SESA can be further diagnosed with the set of attribution simulations. Figures 3c–g show the three-member ensemble mean precipitation change in the simulations driven by the transient natural forcing (NATURAL), anthropogenic forcing (ANTHRO), well-mixed greenhouse gases (GHG), ozone (OZONE), and anthropogenic aerosols (AEROSOL), respectively. In contrast to NATURAL (Fig. 3c), in which the precipitation difference is weak and insignificant across South America, the precipitation change simulated in ANTHRO (Fig. 3d) is nearly the same (in terms of both spatial pattern and amplitude) as that in the historical simulations (Fig. 3b), which demonstrates the dominant role of the anthropogenic forcing in the externally forced summertime precipitation increase in SESA during the twentieth century. Among various anthropogenic forcing agents (Figs. 3e–g), well-mixed greenhouse gases (Fig. 3e) play the leading role in the twentieth-century summertime wetting trend in SESA, while ozone (Fig. 3f) and aerosols (Fig. 3g) do not show

FIG. 3. Difference in the mean precipitation (mm day^{-1}) between two periods, 1981–2010 and 1901–50 over South America in (a) CRU observations and CM2.5 simulations: (b) ALLFORC, (c) NATURAL, (d) ANTHRO, (e) GHG, (f) OZONE, (g) AEROSOL, and (h) CNTL. (i) The projected (RCP8.5 scenario) precipitation change for the period 2070–99 relative to 1901–50 in ALLFORC. The precipitation change in CNTL is computed between the two periods corresponding to the two calendar periods, and is subtracted from all other ensembles to highlight the externally forced signal. Shown for the model is the three-member ensemble mean. The gray-stippled area indicates the difference is not significant based on a two-sided Student's t test at the 5% significance level. The black-dashed boxes indicate the SESA region where the precipitation time series in Fig. 1 is averaged.

any significant impacts. Note that the results obtained here in GFDL CM2.5 differ from those of Gonzalez et al. (2014), who argued for a dominant role of ozone depletion in the summertime positive precipitation trend in SESA during the late twentieth century. Despite a likely model dependence of the results (see more discussion below), we next present a consistent picture of the model's hydrological response to various forcing agents in terms of both dynamics and thermodynamics.

The external radiative forcing enhances the summertime precipitation in SESA via modifying large-scale atmospheric circulation. As part of the subtropical dry zone, the SESA region is located underneath the climatological descending branch of the Southern Hemisphere Hadley cell during austral summer (solid contours in Fig. 4b and dashed contours in Fig. 5b; very similar climatology in ERA-Interim; not

shown). In response to the radiative forcing changes, the climatological atmospheric descending flow over SESA weakens, resulting in anomalous ascending motion and thus more precipitation as seen in ALLFORC (Fig. 4b), ANTHRO (Fig. 4d), and GHG (Fig. 4e). The changes in vertical motion pass the statistical test at the 5% significance level for these three experiments that include well-mixed greenhouse gas forcing changes. In contrast, the corresponding atmospheric vertical motion changes in NATURAL (Fig. 4c), OZONE (Fig. 4f), and AEROSOL (Fig. 4g) are weak and not significant, consistent with the insignificant precipitation changes in SESA (Fig. 3). This contrast provides dynamical evidence in GFDL CM2.5 for the dominant role of greenhouse gases in the externally forced summertime wetting trend in SESA via driving local anomalous ascent.
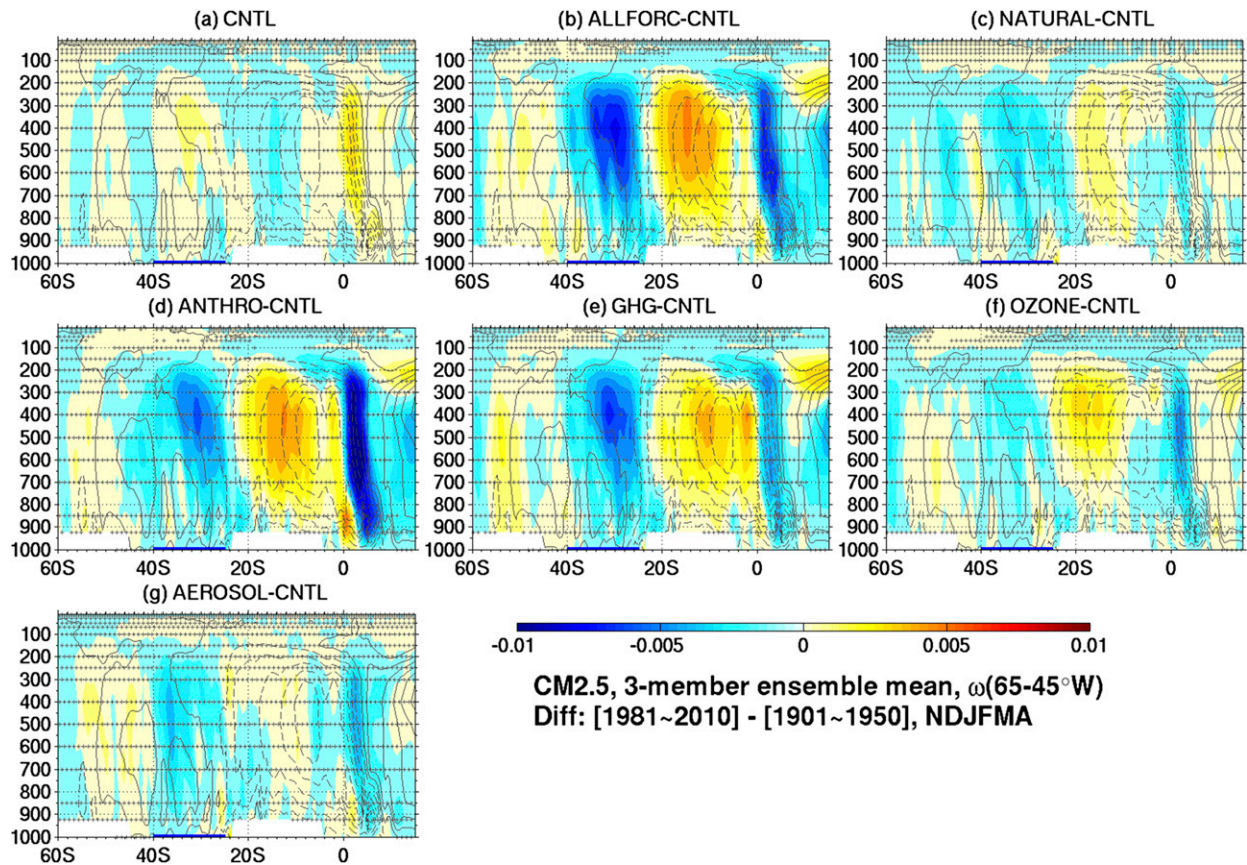
FIG. 4. The latitude–pressure cross section difference (shading) in the pressure velocity (Pa s^{-1}) averaged from 45° to 65°W between two periods, 1981–2010 and 1901–50, over South America in CM2.5 simulations: (a) CNTL, (b) ALLFORC, (c) NATURAL, (d) ANTHRO, (e) GHG, (f) OZONE, and (g) AEROSOL. The difference in CNTL [in (a)] has been subtracted from all the forced simulations in (b)–(g) to highlight the externally forced signal. Contours depict the climatological pressure velocity, with solid indicating zero and positive values (downward motion; contour interval of 0.01 Pa s^{-1}) and dashed indicating negative values (upward motion; contour interval of −0.01 Pa s^{-1}). Shown is the three-member ensemble mean. The gray-stippled area indicates the difference is not significant based on a two-sided Student's t test at the 5% significance level. The blue bars along the x axis indicate the latitudinal range of the SESA region.

The same relationship between precipitation and atmospheric vertical motion changes is also simulated north of SESA. In ALLFORC, ANTHRO, and GHG (Figs. 3b,d,e), the central South American (20°S–0°) drying and the equatorial American moistening are accompanied with anomalous descending motion (20°S–0°) and ascending motion (0°–10°N) (Figs. 4b,d,e), respectively. In the simulations that exclude greenhouse gas changes, the consistency still holds with insignificant changes in both atmospheric vertical motion and precipitation. These results lend further support to the role of well-mixed greenhouse gases in driving summertime atmospheric dynamical and hydrological changes during the twentieth century across South America in GFDL CM2.5.

The changes in atmospheric circulation over South America are part of the poleward shift of the global-scale atmospheric circulation in response to external radiative forcing changes, which has been reported in a number of previous studies (e.g., Kushner et al. 2001; Yin 2005; Bengtsson et al. 2006; Seager et al. 2007). The poleward shift of the Southern Hemisphere summertime atmospheric circulation is clearly manifested by changes in the meridional overturning circulation (Fig. 5b; e.g., Hadley and Ferrel cells), zonal jets (Fig. 6b; e.g., midlatitude jets), and other atmospheric fields such as sea level pressure (not shown); in GFDL CM2.5, the poleward shift is caused primarily by the radiative forcing associated with increased greenhouse gases (Figs. 5b,d,e and 6b,d,e). Other transient forcing agents, including ozone and aerosols, do not show any significant impacts on the tropospheric circulation for this particular model (Figs. 5f,g and 6f,g; see below for more discussion). We note that the poleward shift of the Southern Hemisphere atmospheric circulation is simulated not only during austral summer (NDJFMA) but also during austral winter (May through October) with a comparable magnitude; however, the
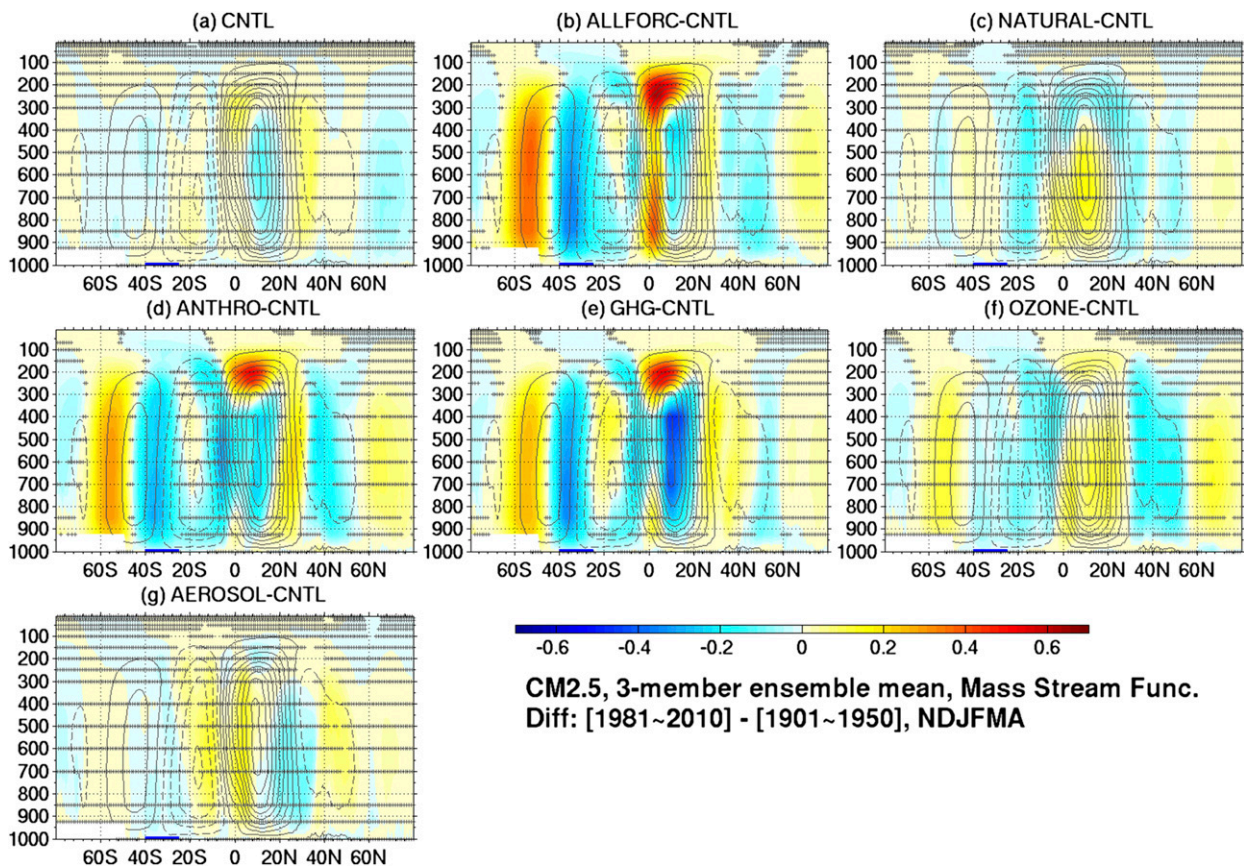
FIG. 5. As in Fig. 4, but for the zonal mean atmospheric mass streamfunction (10^{10} kg s^{-1}). The changes are in shading, and the long-term climatology is in contours with the solid lines (starting at 1×10^{10} kg s^{-1}, contour interval of 2×10^{10} kg s^{-1}) indicating clockwise circulation and the dashed lines (starting at -1×10^{10} kg s^{-1}, contour interval of -2×10^{10} kg s^{-1}) counterclockwise circulation.

poleward shift is more zonally uniform during summer than during winter (not shown).

The different dynamical responses of the atmosphere in CM2.5 to various external forcing agents likely arise from the different atmospheric thermodynamic responses, particularly in the troposphere. Figure 7 illustrates the corresponding changes in zonal mean atmospheric temperature. ALLFORC, ANTHRO, and GHG simulate similar atmospheric temperature changes, including stratospheric cooling, overall tropospheric warming, and amplified warming in both the tropical upper troposphere and the northern polar lower troposphere. In contrast, OZONE simulates a much weaker tropospheric warming (despite the similar stratospheric cooling to ALLFORC and ANTHRO), while NATURAL and AEROSOL simulate the opposite tropospheric cooling. The similarities among ALLFORC, ANTHRO, and GHG as well as their differences from OZONE, NATURAL, and AEROSOL suggest that the tropospheric temperature changes, in response primarily to increased well-mixed greenhouse gases, play a key role in the poleward shift of the

Southern Hemisphere summertime atmospheric circulation during the twentieth century. One interpretation is that the enhanced tropospheric static stability in low latitudes, an established result of moist thermodynamics, suppresses the baroclinic instability that sustains the subtropical jets at the poleward flank of the Hadley cell, thus pushing the subtropical jets poleward (to a new latitude where the static stability change does not negate the baroclinic instability) and leading to expansion of the Hadley cell (e.g., Walker and Schneider 2006; Lu et al. 2007). In addition to the slow adjustment in the tropospheric static stability, a faster dynamical adjustment involving troposphere–stratosphere coupling may also play a role in the tropical expansion. As a transient response to the increased greenhouse gases, the stratospheric westerly acceleration propagates downward and enhances upper-troposphere transient eddy moment flux convergence, which drives the poleward shift of the subtropical jets (Wu et al. 2012, 2013).

The weak dynamical response of CM2.5 to the transient ozone forcing disagrees with the previous findings by Kang et al. (2011), Polvani et al. (2011), and Gonzalez
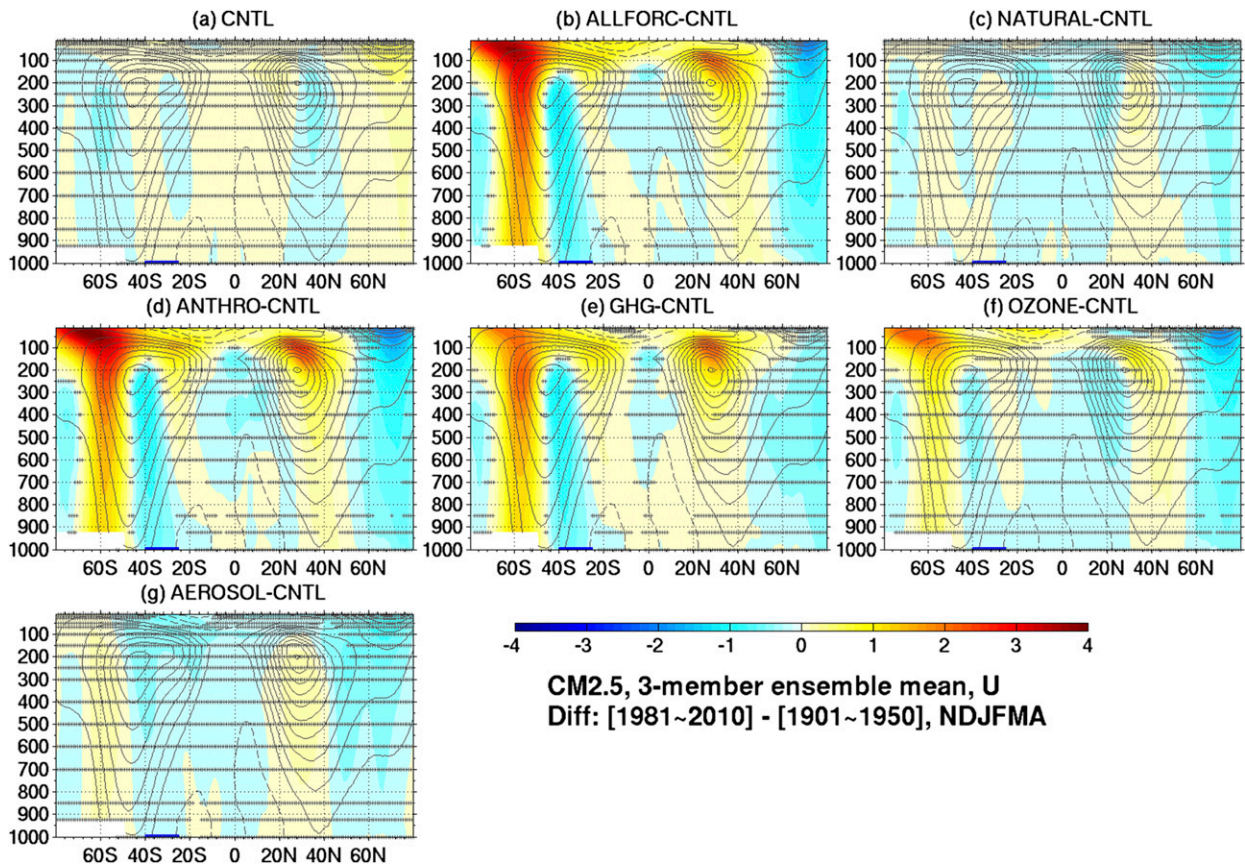
FIG. 6. As in Fig. 4, but for zonal mean zonal wind component (m s^{-1}). The changes are in shading, and the long-term climatology is in contours with the solid lines (starting at 4 m s^{-1}, contour interval of 4 m s^{-1}) indicating eastward winds and the dashed lines (starting at -4 m s^{-1}, contour interval of -4 m s^{-1}) westward winds.

et al. (2014), who found, using different climate models, that the stratospheric ozone depletion can drive the poleward shift of the Southern Hemisphere summer-time atmospheric circulation during the twentieth century. The reason for the intermodel difference of ozone impacts is beyond the scope of the current study; nonetheless, the weak dynamical response of CM2.5 to the ozone forcing, if weaker than the unknown actual response in nature, could contribute to the amplitude discrepancy between the observed and simulated twentieth-century summertime positive rainfall trend in SESA (recall Fig. 3).

2) ROLE OF INTERNAL CLIMATE VARIABILITY

In addition to anthropogenic radiative forcing, low-frequency internal variability of the coupled climate system likely also contributes to the observed summer-time moistening trend in SESA during the twentieth century. To assess the potential role of internal vari-ability, we compute the spread of the simulated pre-cipitation change among the ensemble members against the probability distribution of the precipitation change

caused only by internal variability in CM2.5. The prob-ability distribution is constructed with a Monte Carlo technique by repeating the following sampling process 10 000 times: we first randomly select a 30-yr period and a nonoverlapping 50-yr period (to mimic 1981–2010 and 1901–50) from the last 1000 years of the control simulation, and then calculate the summertime pre-cipitation difference in SESA between the two periods. The result is shown in Fig. 8a. The possible precipitation changes caused by internal variability in CM2.5 between a 30-yr period and a 50-yr period exhibit a Gaussian-like distribution (expected from the central limit theorem) with a range of about 0.48 mm day^{-1}. Given the small size of the CM2.5 ensembles, the spread among the members of each ensemble—reflecting the internal variability—is about half of the possible range (e.g., 0.24 mm day^{-1} for ALLFORC; black dots), high-lighting the need for large-number ensembles to better resolve internal variability. Nonetheless, the spread among the ensemble members suggests a role for low-frequency internal variability such as the AMO (Seager et al. 2010; Ruprich-Robert et al. 2016, manuscript
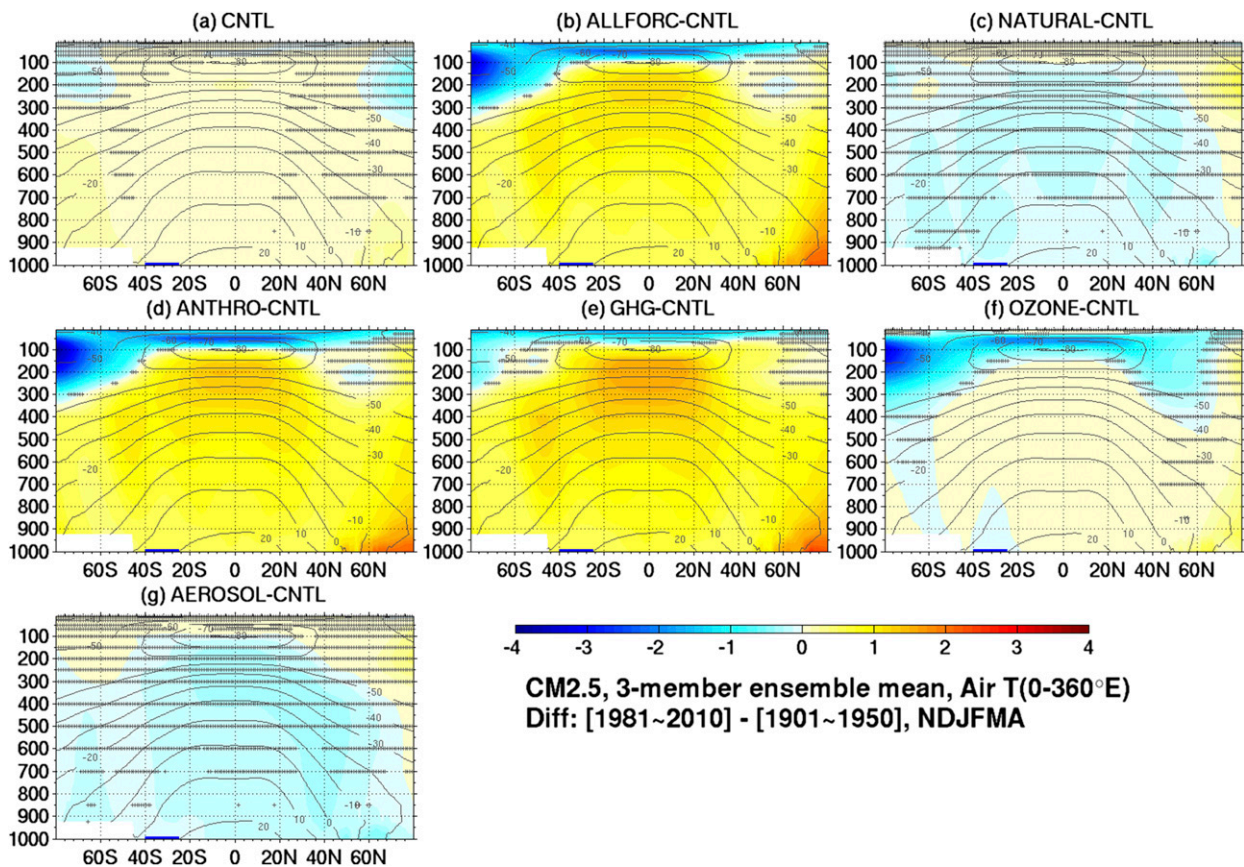
FIG. 7. As in Fig. 4, but for zonal mean atmospheric temperature (°C). The changes are in shading, and the long-term climatology is in contours.

submitted to *J. Climate*) or PDV (e.g., Huang et al. 2005) in the twentieth-century summertime precipitation changes in SESA; this low-frequency internal variability likely contributes (at least partly) to the amplitude discrepancy between the observed and simulated ensemble mean summertime moistening trend in SESA (recall Fig. 3).

The observed precipitation change (black diamond), 0.67 mm day^{-1}, is far outside of the possible range caused by internal variability in CM2.5, which suggests that either 1) the radiative forcing plays a dominant role in the observed twentieth-century summertime moistening trend in SESA or 2) CM2.5 may underestimate the observed internal variability on multidecadal time scales (or perhaps both are true). The second hypothesis is hard to test because of both the relatively short record of observations and the challenge to cleanly extract internal variability from observations; if true, it would also contribute to the amplitude discrepancy between the observed and simulated summertime precipitation trend in SESA. As to the first hypothesis, CM2.5 does demonstrate a substantial role for anthropogenic radiative forcing associated with greenhouse gases, which is

highlighted by the result in Fig. 8a that two of the five ALLFORC members (black dots), one of the three ANTHRO members (magenta dots), and all three GHG members (red dots) fall outside the distribution range of the internal variability, while all OZONE (cyan dots), AEROSOL (blue dots), and NATURAL (green dots) members are inside the range. The fact that all five ALLFORC members simulate smaller changes than the observations implies either that the ensemble size is too small to represent the full range of internal variability or that CM2.5 underestimates the observed change owing to its weak response to ozone depletion and/or possible weak multidecadal internal variability (the second hypothesis).

To better quantitatively estimate the relative role of internal climate variability and external radiative forcing, we make use of the 30- and 35-member ensembles performed with FLOR-FA and repeat the above probability analysis. Since these large ensembles start in 1941, we focus on the precipitation change of the same 1981–2010 period relative to the period 1951–70 (as opposed to 1901–50). Using the latter period in the CM2.5 suite does not change the main conclusions
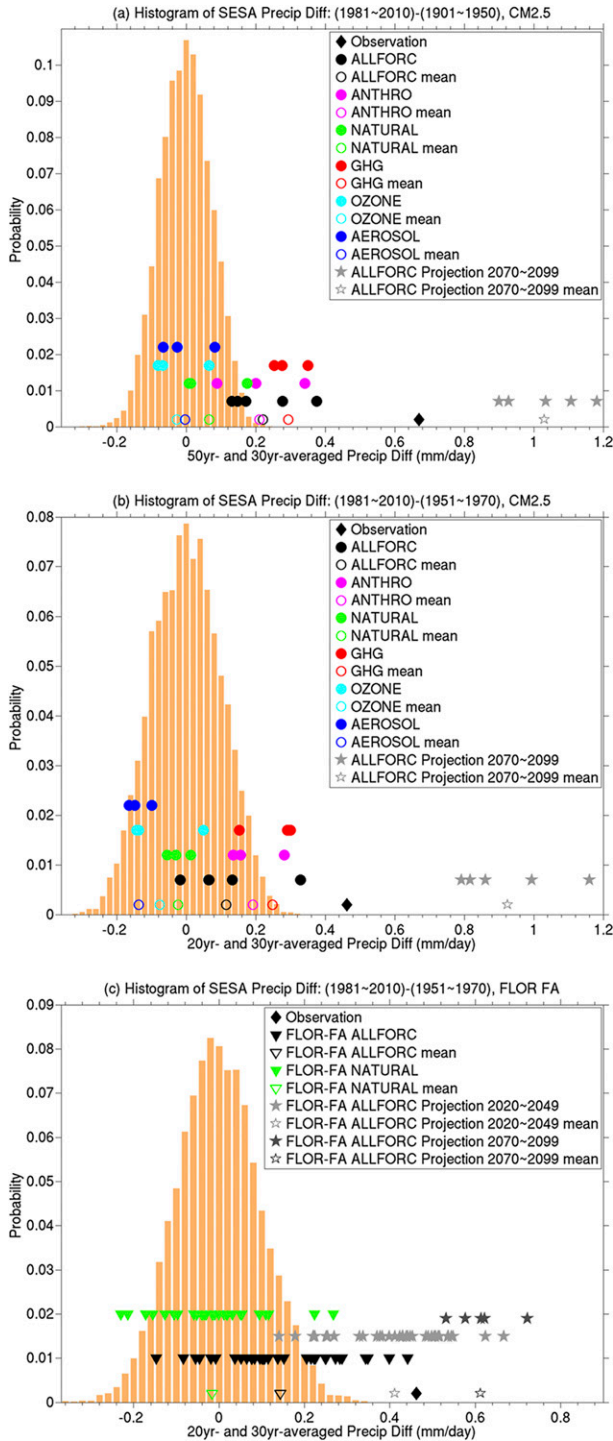
FIG. 8. (a) Probability distribution (histogram) of the difference in the SESA summertime precipitation between a 50-yr period and a 30-yr period based on the last 1000 yr of the 1100-yr CM2.5 CNTL with a Monte Carlo technique (see text for details), the simulated precipitation change for 1981–2010 relative to 1901–50 in the individual forced simulations (colored dots; open circles indicate ensemble mean) as well as the projected precipitation change for 2070–99 relative to 1901–50 in the ALLFORC simulations

drawn from using the earlier period: as in Fig. 8a, Fig. 8b shows that 1) the spread among each forced ensemble (e.g., 0.35 mm day^{-1} in ALLFORC, black dots) is about half or less than half of the possible range caused by the internal variability in CM2.5 (0.67 mm day^{-1}); 2) compared to the ensembles that do not include increased greenhouse gases (NATURAL, OZONE, and AEROSOL), the ensembles that include increased greenhouse gases (ALLFORC, ANTHRO, and GHG) mostly cluster to the positive side of the probability distribution; and 3) the observed rainfall change (black diamond, 0.46 mm day^{-1}, smaller than the 0.67 mm day^{-1} in Fig. 8a) is outside the range of the possible rainfall changes caused by internal variability. Besides these similarities between Figs. 8a and 8b, there are two notable but expected differences: 1) the internal variability range in Fig. 8b is wider than that in Fig. 8a, resulting from using the 20-yr average as opposed to the 50-yr average (the latter removes more internal variability), and 2) the rainfall changes in AEROSOL (blue dots) cluster to the negative side of the probability distribution in Fig. 8b, as a result of the stronger emission of anthropogenic aerosols during the second half of the twentieth century than the first half (as reported in the fifth IPCC report; recall the cooling effect of aerosols on the troposphere in Fig. 7g). The consistency between using two different periods in the same CM2.5 suite further substantiates the role of both anthropogenic forcing and internal variability, and meanwhile provides confidence to examine the large ensembles of FLOR-FA using the later 1951–70 period.

←

responding to the RCP8.5 forcing (gray stars; unfilled indicate ensemble mean). Before constructing the histogram, the model drift in CNTL (about a 0.25 mm day^{-1} increase over 1000 yr based on a linear regression) is removed by a low-pass filter with a cutoff period of 200 yr. The corresponding model drift from CNTL is also subtracted from each forced simulation. (b) As in (a), but for the difference between 20-yr and 30-yr periods in CNTL, the simulated change for 1981–2010 relative to 1951–70 in the forced simulations (colored dots) and the projected (RCP8.5 scenario) change for 2070–99 relative to 1951–70 (gray stars). (c) As in (b), but using the two large ensembles of FLOR-FA (35 members of ALLFORC in black triangles and 30 members of NATURAL in green triangles). In (c), the light gray stars denote the projected rainfall change by the 35-member ALLFORC for 2020–49 relative to 1951–70 in response to the RCP4.5 forcing, while the dark stars indicate the projected (RCP4.5 scenario) rainfall change by the 5 long ALLFORC members for 2070–99 relative to 1951–70. The probability distribution in (c) is constructed from the model years 101–1100 (1000 yr) of the 3500-yr FLOR-FA control simulation, whose model drift (a linear increase of 0.21 mm day^{-1} over 1000 yr) has also been subtracted from both the control and forced simulations (aligned with the control run based on their ocean component initialized at 1941).

(a) Histogram of SESA Precip Diff: (2001~2011)-(1979~2000), FLOR FA

(b) Histogram of Diff between two 35-mem ensemble means of Precip Diff
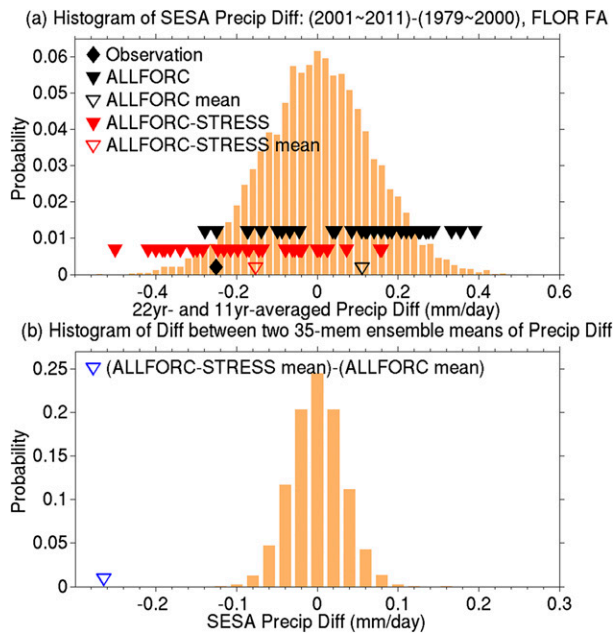
FIG. 9. (a) As in Fig. 8c, but for the difference between the summertime precipitation averaged for 1979–2000 and 2001–11 in CRU observations (black diamond), FLOR-FA ALLFORC (black triangles), and ALLFORC_STRESS simulations (red triangles). (b) Blue unfilled triangle denotes the difference between ensemble means of FLOR-FA ALLFORC_STRESS [red unfilled triangle in (a)] and FLOR-FA ALLFORC [black unfilled triangle in (a)], whereas the histogram illustrates the probability distribution of the difference in ensemble mean between two ensembles (based on 10 000 samples), with each ensemble consisting of 35 members and each member being the rainfall change averaged over a 22-yr period relative to a nonoverlapping 11-yr period randomly chosen from the 1000-yr FLOR-FA CNTL. Note that (b) indicates the significance of the difference between FLOR-FA ALLFORC and FLOR-FA ALLFORC_STRESS with regard to the probability of the difference caused by internal variability in FLOR-FA.

The possible range of the precipitation change caused by internal variability in FLOR-FA (Fig. 8c) is comparable to that in CM2.5 (Fig. 8b), both about 0.67 mm day^{-1}. However, with the two large ensembles, the internal variability in FLOR-FA is much better resolved, with a spread of 0.50 mm day^{-1} among the NATURAL ensemble (filled green triangles) and a spread of 0.59 mm day^{-1} among the ALLFOR ensemble (filled black triangles). The 30 NATURAL simulations cluster around the center of the probability distribution with an ensemble mean of −0.02 mm day^{-1} (unfilled green triangle, reflecting the impacts of the radiative forcing due natural processes), while the 35 ALLFORC simulations cluster to the positive side of the probability distribution with an ensemble mean of 0.14 mm day^{-1} (unfilled black triangle, indicating the impacts of the total radiative forcing due to both natural and anthropogenic processes). This difference between the two

ensembles highlights the role of anthropogenic radiative forcing. With the ensemble mean difference of 0.16 mm day^{-1}, the anthropogenic radiative forcing in FLOR-FA explains only about 35% of the observed summertime rainfall increase (0.46 mm day^{-1}) in SESA during 1981–2010 relative to 1951–70. It is certainly possible that FLOR-FA underestimates the role of anthropogenic radiative forcing, such as the weaker response to ozone changes in CM2.5 than in some other climate models. We note that the largest rainfall change simulated by the ALLFORC ensemble is 0.44 mm day^{-1}, 96% of the observed increase, which suggests that FLOR-FA is capable of simulating the observed multidecadal regional rainfall changes. Although it is possible that this ALLFORC member may still underestimate the role of anthropogenic radiative forcing by overestimating the role of other processes (such as internal variability), it is also plausible that the majority of the observed summertime rainfall increase in SESA after 1950 is attributed to the internal climate variability, such as the PDV and AMO that have been shown to play an important role in the observed rainfall increase during the late twentieth century (Huang et al. 2005; Seager et al. 2010; Ruprich-Robert et al. 2016, manuscript submitted to *J. Climate*).

b. Precipitation decline during the first decade of the twenty-first century

The atmospheric concentration of greenhouse gases, particularly carbon dioxide, has been continuously increasing during the past several decades, and both CM2.5 and FLOR-FA simulate a continuous summertime moistening trend in SESA in response to this increase. In contrast, the observed summertime rainfall in SESA shows a decline during the first decade of the current century. What causes the observed decadal rainfall decline? Here we show that this observed drying is largely driven by recent trade wind strengthening in the tropical Pacific.

Based on a suite of experiments performed with FLOR-FA, Delworth et al. (2015) show that the observed changes of the Pacific trade winds likely drive the North American drought during the last decade by inducing tropical Pacific cooling and the subsequent atmospheric teleconnection. Here we hypothesize that changes in the tropical Pacific play a similar role in driving the summertime rainfall decline in SESA during the last decade. To test this hypothesis, we make use of the suite of experiments from Delworth et al. (2015) and analyze the response of the summertime precipitation change in SESA to the tropical Pacific trade wind strengthening. Figure 9a shows the observed and simulated precipitation changes between 2001–11 and 1979–2000 against the probability distribution of the precipitation change
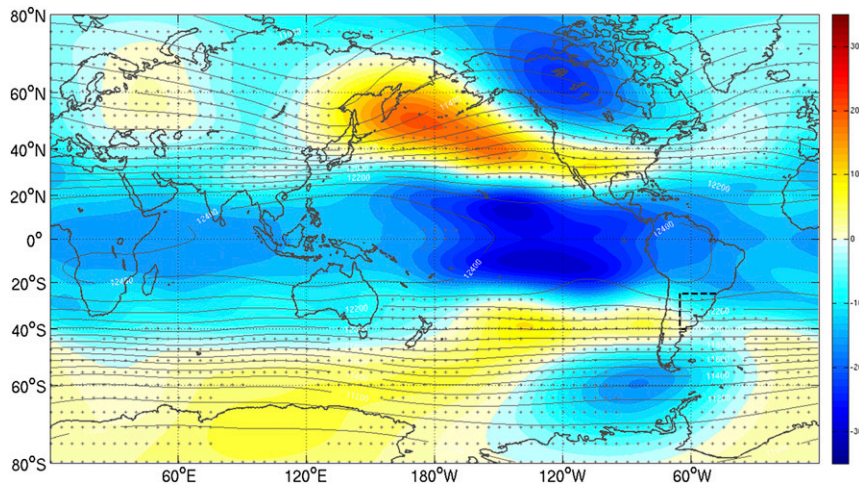
FIG. 10. The 200-hPa geopotential height (m) response to the imposed wind stress anomalies in the tropical Pacific averaged for the period 2000–11 during austral summer (NDJFMA). The shading denotes the geopotential height difference of ALLFORC_STRESS relative to ALLFOR and contours are the corresponding climatology in ALLFORC. Gray-dotted area means the response is not significant at 5% significance level based on a two-sided Student's *t* test.

between an 11-yr period and a nonoverlapping 22-yr period caused by internal variability in FLOR-FA control simulations. On decadal time scales, the possible precipitation changes caused by internal variability exhibit a range of about 1 mm day^{-1} (larger than that on multidecadal time scales, as expected). The observed change (black diamond), -0.25 mm day^{-1}, falls inside the range, which suggests that internal variability by itself is capable of generating the observed rainfall decline. The 35 ALLFORC members driven only by radiative forcing (filled black triangles) cluster to the positive side of the probability distribution, with an ensemble mean moistening of about 0.11 mm day^{-1} (unfilled black triangle), which is consistent with the role of radiative forcing in enhancing the summertime rainfall in SESA. In contrast, the 35 ALLFORC_STRESS members driven additionally by imposed wind stress anomalies in the tropical Pacific (filled red triangles) group to the drying side of the probability distribution, with the ensemble mean (-0.15 mm day^{-1}, unfilled red triangle) explaining about 60% of the observed rainfall decline.

How significant is the difference between the ensemble means of ALLFORC_STRESS and ALLFORC (i.e., -0.26 mm day^{-1})? The probability distribution of an equivalent difference caused by internal variability in FLOR-FA is shown in Fig. 9b, where the equivalent difference is between ensemble means of two ensembles of 35 members with each member being the rainfall change averaged over a 22-yr period relative to a nonoverlapping 11-yr period randomly chosen from the 1000-yr control simulation. The difference in the ensemble mean between

ALLFORC_STRESS and ALLFORC (blue unfilled triangle) is far outside the possible range of the equivalent difference caused by internal variability (-0.12–0.15 mm day^{-1}, based on 10 000 samples), demonstrating a significant role of the anomalous momentum flux imposed in the tropical Pacific. This result, along with those shown in Fig. 9a, suggests that the trade wind strengthening in the tropical Pacific plays a leading ($\sim$60%) role in the recent summertime rainfall decline in SESA.

The physical process that links the tropical Pacific trade winds to SESA precipitation is the atmospheric teleconnection, an established mechanism of ENSO impacting the global climate. In response to the strengthened trade winds, the resultant surface cooling induces an upper-tropospheric trough in the tropics, which then excites a Rossby wave train that propagates poleward and eastward and projects an anomalous ridge over southern South America (about 30°–50°S; Fig. 10); this ridge results in anomalous downdrafts and thus the rainfall decline in SESA.

Will the recent decadal rainfall decline in SESA continue? Climate models project weakening in the tropical atmospheric circulation including the Pacific trade winds in response to the global warming associated with changing radiative forcing (e.g., Vecchi et al. 2006). The recent Pacific trade wind strengthening is therefore not likely a response to the radiative forcing, but a result of internal variability such as the Pacific decadal variability. This speculation implies that the Pacific trade winds will swing back to the normal strength and even weaken. If this phase transition were to occur in the near future, we would expect the summertime moistening
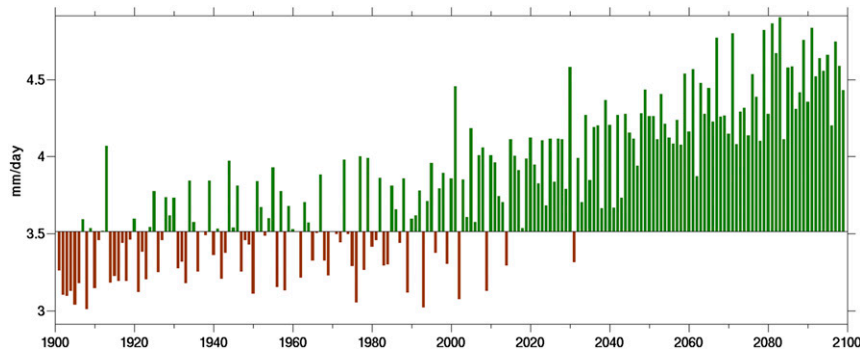
FIG. 11. Simulated summertime (NDJFMA) precipitation in SESA in CM2.5 ALLFOR, five-member ensemble mean (RCP8.5 forcing after year 2006). The brown (green) bars indicate that the SESA summertime precipitation is below (above) the 1901–2012 climatological mean.

trend in SESA to resume in response to the combined effects of the relaxed (or weakened) Pacific trade winds and increasing radiative forcing.

c. Projection of summertime precipitation change in SESA

With anthropogenic radiative forcing and internal climate variability both contributing to summertime rainfall variability in SESA, how will the SESA summertime rainfall evolve in the future? First, we project future rainfall changes in South America toward the end of the current century by using the ensemble of the 1861–2100 ALLFORC simulations performed with CM2.5 driven by radiative forcing in the RCP8.5 emission scenario. We find that on centennial time scales the precipitation change is much less sensitive to the ensemble size. To be consistent with the attribution ensembles, we show the ensemble mean of the three ALLFORC members in Fig. 3i. In response to the high-end RCP8.5 scenario of changes in radiative forcing, the twentieth-century summertime precipitation changes in South America simulated in CM2.5 will be amplified by the end of the current century (cf. Figs. 3b and 3i). These amplified precipitation changes, significant at the 5% level, include the drying trend in central and southern South America and the moistening trend in equatorial South America and SESA. Consistent amplification (not shown) is simulated in the changes of atmospheric circulation and temperature fields illustrated in Figs. 4b, 5b, 6b, and 7b. Using the five-member FLOR-FA 1861–2100 ensemble driven by radiative forcing of the medium RCP4.5 emission scenario, we obtain a similar pattern of future rainfall changes but with expected smaller amplitude (not shown). These results demonstrate the crucial role of radiative forcing associated with the anthropogenic greenhouse gases in the long-term changes of rainfall on regional scales.

To characterize the role of internal climate variability in future rainfall changes, we present the spread of the projected summertime rainfall changes in SESA among the individual members of the ALLFORC ensemble in Figs. 8a–c. The internal variability—an unpredictable source—will continue to impact the future rainfall changes. It adds substantial uncertainty to the near-term projection (2020–49) of the summertime rainfall changes in SESA (Fig. 8c, light gray stars), suggesting a crucial role for internal variability in regional rainfall changes on decadal-to-multidecadal time scales. However, for the long-term projection (2070–99), the spread caused by internal variability is smaller than the ensemble mean that arises mostly from the anthropogenic radiative forcing (light gray stars in Figs. 8a,b and dark stars in Fig. 8c, versus the corresponding unfilled stars), which suggests a dominant role for the anthropogenic forcing in regional rainfall changes on centennial and longer time scales. To highlight the relative role of internal variability and external forcing, we show the ensemble mean of the time series of summertime rainfall in SESA simulated by CM2.5 ALLFORC in Fig. 11. During the twentieth century, the ensemble mean time series, despite removing some internal variability, still exhibits substantial interannual-to-multidecadal variability (partly because of the small ensemble size), whereas during the twenty-first century a positive trend caused by anthropogenic radiative forcing dominates the SESA summertime rainfall variability. This enhanced long-term rainfall increase will challenge the regional socioeconomic development by potentially increasing the risk of floods.

4. Summary and discussion

Using the GFDL high-resolution global CM2.5 and its variant FLOR-FA, we investigated the physical mechanisms underlying the decadal-to-multidecadal changes of summertime rainfall in southeastern South America

(SESA) observed since the beginning of the twentieth century. Compared to the lower-resolution CM2.1, CM2.5 improves the simulation of regional hydroclimate in many regions including South America, thereby increasing our confidence in the utility of this model for the detection, attribution, and projection of hydroclimate changes on regional scales.

The observed low-frequency changes of summertime rainfall in SESA exhibits two distinctive features: a twentieth-century multidecadal moistening trend of varying rates with the largest rate observed during the last three decades (1970–2000) and a contrasting drying trend during the first decade of the current century. To assess the physical processes underlying these low-frequency variations, we analyzed two suites of experiments, performed respectively with CM2.5 and FLOR-FA, that are systematically designed for detection, attribution, and projection of climate change on various spatiotemporal scales.

The twentieth-century multidecadal positive trend of summertime rainfall in SESA is reproduced by the CM2.5 historical simulations, although with a smaller magnitude than observed. The simulated positive trend is attributed to radiative forcing changes associated with increasing concentrations of well-mixed greenhouse gases. The radiative forcing drives a poleward shift of the Southern Hemisphere summertime atmospheric circulation. In particular, the subtropical descending branch of the tropical Hadley cell moves poleward away from SESA, which leads to anomalous ascent and therefore wetter conditions in SESA (and presumably other regions at similar latitudes). Other forcing agents, such as natural and anthropogenic aerosols and stratospheric ozone, do not show significant impacts on the tropospheric temperature and circulation and therefore hydroclimate across South America. The weak response to aerosols is likely due to the fact that CM2.5 does not include aerosol indirect effects that can influence cloud feedback and precipitation; incorporating indirect effects into the model may enhance the impacts of natural and anthropogenic aerosols on atmospheric circulation and regional hydroclimate. Regarding ozone, CM2.5 shows a strong response in the stratosphere over the Southern Hemisphere where the ozone changes (depletion) are the largest, but a weak insignificant response in the troposphere (both thermodynamics and dynamics). This result, particularly the tropospheric response, is in contrast to a few previous studies (Kang et al. 2011; Polvani et al. 2011) that, based on different climate models, suggested a primary role for ozone depletion in driving the twentieth-century changes of the Southern Hemisphere summertime atmospheric circulation

(including the troposphere). This disagreement suggests that climate models have distinctive sensitivities in the tropospheric response to stratospheric ozone changes, and highlights the urgent need of examining these sensitivities against the limited observations in order for a better understanding of observed climate changes. The weak response of CM2.5 to ozone forcing, if weaker than the unknown actual response in nature, may contribute to the amplitude discrepancy between the observed and simulated summertime rainfall changes in SESA during the twentieth century.

Besides the weak response to aerosols and ozone, another source for the amplitude discrepancy is the low-frequency internal variability of the coupled climate system that is (at least) partly removed from the ensemble average. The spread among the ensemble members suggests a role for internal variability in contributing to the observed summertime moistening trend in SESA. The likely candidates for low-frequency internal variability include the AMO and the PDV. In particular, the tropical cold SST anomalies associated with the negative phase of the AMO from the early 1960s to the late 1990s have been argued to be responsible for the wetter conditions during the late twentieth century (Seager et al. 2010). A new numerical study by Ruprich-Robert et al. (2016, manuscript submitted to *J. Climate*) using CM2.1 and Community Earth System Model version 1 also found a moistening response to the negative phase of the AMO. These studies, along with the fact that the AMO was in its negative phase from the late 1960s through the mid-1990s, when the SESA summertime precipitation was increasing, suggest that the AMO should have contributed to the enhanced summertime rainfall in SESA during the late twentieth century. In addition, the warm phase of the PDV during the two decades following the 1976/77 climate shift has also been shown to contribute to the wetter conditions in SESA (Huang et al. 2005). Besides the contribution from these internal modes of variability to the observed precipitation changes that may not be well simulated by CM2.5, it is also possible that the model may underestimate observed internal variability. This possibility, although hard to test owing to the relatively short record of observations and the challenge to cleanly extract the associated internal variability, can contribute to the amplitude discrepancy between the observed and simulated summertime precipitation changes in SESA.

We have also examined the twentieth-century summertime rainfall changes in SESA using CMIP5 historical simulations (Taylor et al. 2012) (Fig. 12). We find that the CMIP5 ensemble can reproduce some aspects of the observed summertime rainfall increase. As is the
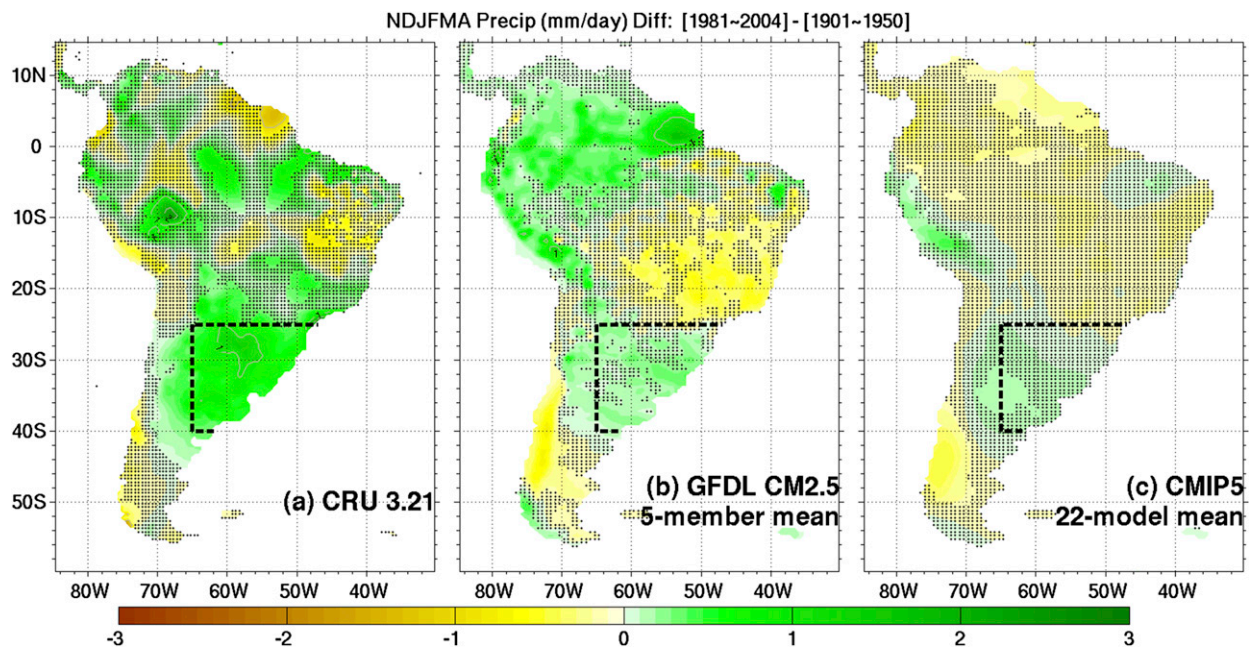
FIG. 12. Comparison of the twentieth-century summertime (NDJFMA) rainfall change over South America among (a) CRU observations, (b) GFDL CM2.5 (5-member average), and (c) CMIP5 models (22-model average). The rainfall change is assessed as the difference in rainfall averaged during 1981–2004 relative to 1901–50. All model simulations are in historical configuration. The CMIP5 models (acronym expansions available online at http://www.ametsoc.org/PubsAcronymList) used here include BCC_CSM1.1 (3), BCC_CSM1.1(m) (3), BNU-ESM (1), CCCma CanESM2 (10), CSIRO–BoM ACCESS1.0 (10), CSIRO Mk3.6.0 (50), FIO-ESM (4), INM-CM4.0 (2), IPSL-CM5A-LR (7) and IPSL-CM5A-MR (3), LASG/IAP FGOALS-s2 (3), MIROC ESM (8) and MIROC5 (11), MPI-M ESM (14), MRI CGCM3 (10), NCAR CCSM4 (43), NCAR CESM1(BGC) (3), NCAR CESM1(CAM5.1-FV2) (4), NCAR CESM1 (CAM5) (10), NCAR CESM1(FASTCHEM) (12), NCAR CESM1(WACCM) (4), and Norwegian Climate Centre NorESM1-ME (8), where the number inside parentheses after each model indicates the ensemble size for that model. The precipitation outputs in CMIP5 models are linearly interpolated onto the same grid as in CM2.5 to compute the multimodel mean. The gray stippling indicates that rainfall change is not significant, where the significance in (a) and (b) is defined as in Fig. 3 and in (c) is defined when 11 or more models simulate significant (defined as in Fig. 3) rainfall changes. The black-dashed areas indicate the SESA region.

case for the GFDL CM2.5 ALLFORC ensemble mean, the CMIP5 multimodel mean of rainfall changes (1981–2004 relative to 1901–50) over South America captures some of the spatial pattern of observed rainfall changes south of about 20°S, including the SESA moistening and the drying southwest of SESA (less significant), but has a smaller magnitude than that in both CM2.5 and observations (Figs. 12a,b vs Fig. 12c). The weak CMIP5 multimodel mean likely arise from a number of reasons: 1) it excludes at least part of rainfall changes caused by internal variability (averaging across 223 simulations from 22 climate models), 2) there is a large spread among the CMIP5 models in their simulated SESA summertime rainfall changes (not shown), and 3) most of the CMIP5 models underestimate the observed summertime moistening trend in SESA (Gonzalez et al. 2014). Despite the weak magnitude of the CMIP5 multimodel mean, used widely to quantify the contribution from external radiative forcing, the result shown in Fig. 12 (particularly in terms of the spatial pattern) highlights the CMIP5 consensus on the role of external

radiative forcing in observed rainfall changes over South America (south of 20°S) during the last century. It is noteworthy that all the 22 CMIP5 models (refer to the website http://cmip-pcmdi.llnl.gov/cmip5/availability.html for details) have a coarser atmospheric spatial resolution (ranging from about 3° to 1° latitude/longitude) than CM2.5, but are still capable of—at least partly—simulating regional rainfall changes caused by external radiative forcing.

Following the positive rainfall trend in SESA over the twentieth century, a decline in rainfall began around the year 2000. CM2.5 simulates a continuous positive trend into the twenty-first century in response to radiative forcing. However, when the historical simulations are additionally driven by the observation-based trade wind variations in the tropical Pacific, the rainfall decline is largely replicated. The underlying physical processes are analogous to those in Huang et al. (2005) and Delworth et al. (2015). The observed decadal Pacific trade wind strengthening after the 1997/98 El Niño event drives the persistent cooling of the tropical Pacific, which dries SESA via La Niña–like

atmospheric teleconnection. These results demonstrate a crucial role for the tropical Pacific climate in the rainfall changes in SESA on decadal time scales.

Another possible contribution to the recent rainfall decline in SESA is from the AMO, which has been in a positive phase since the beginning of the current century. The associated tropical Atlantic warming may also play a role in the recent rainfall decline in SESA. This hypothesis, along with the relative importance of the tropical Pacific and Atlantic climate changes in rainfall variability in SESA, needs further investigation.

The Pacific trade wind strengthening during the past decade is likely related to Pacific decadal variability, since climate models project a weakening of the tropical Pacific trade winds in response to radiative forcing (e.g., Vecchi et al. 2006; Vecchi and Soden 2007; DiNezio et al. 2013). This implies that the tropical Pacific will eventually transition to a neutral or warm state (such a transition might already be underway according to the latest Pacific decadal oscillation index; https://www.ncdc.noaa.gov/teleconnections/pdo/). Our results suggest that when such a transition occurs the positive trend of the summertime rainfall in SESA will resume. On longer time scales toward the end of the current century, in response to a high-end emission scenario (RCP8.5), the CM2.5 projects an amplified pattern of the twentieth-century precipitation changes across South America, including the enhanced moistening in equatorial and southeastern South America (Fig. 11) and enhanced drying in central and southern South America. These projected future rainfall changes suggest an increasing risk of floods and droughts, which would pose more challenges for regional water and food security as well as agriculture and socioeconomic development. The implication is that, despite the dominance of radiative forcing for regional rainfall changes on centennial and longer time scales, low-frequency internal variability plays an equal or larger role on decadal and even multidecadal time scales, and therefore needs to be fully resolved in the efforts of improving the decadal climate prediction.

REFERENCES

Bengtsson, L., K. I. Hodges, and E. Roeckner, 2006: Storm tracks and climate change. *J. Climate*, **19**, 3518–3543, doi:10.1175/JCLI3815.1.

Boisier, J. P., R. Rondanelli, R. D. Garreaud, and F. Muñoz, 2016: Anthropogenic and natural contributions to the southeast Pacific precipitation decline and recent megadrought in central Chile. *Geophys. Res. Lett.*, **43**, 413–421, doi:10.1002/2015GL067265.

Delworth, T. L., and F. Zeng, 2014: Regional rainfall decline in Australia attributed to anthropogenic greenhouse gases and ozone levels. *Nat. Geosci.*, **7**, 583–587, doi:10.1038/ngeo2201.

——, and Coauthors, 2006: GFDL's CM2 global coupled climate models. Part I: Formulation and simulation characteristics. *J. Climate*, **19**, 643–674, doi:10.1175/JCLI3629.1.

——, and Coauthors, 2012: Simulated climate and climate change in the GFDL CM2.5 high-resolution coupled climate model. *J. Climate*, **25**, 2755–2781, doi:10.1175/JCLI-D-11-00316.1.

——, F. Zeng, A. Rosati, G. A. Vecchi, and A. T. Wittenberg, 2015: A link between the hiatus in global warming and North American drought. *J. Climate*, **28**, 3834–3845, doi:10.1175/JCLI-D-14-00616.1.

DiNezio, P. N., G. A. Vecchi, and A. C. Clement, 2013: Detectability of changes in the Walker circulation in response to global warming. *J. Climate*, **26**, 4038–4048, doi:10.1175/JCLI-D-12-00531.1.

Gill, A. E., 1980: Some simple solutions for heat-induced tropical circulation. *Quart. J. Roy. Meteor. Soc.*, **106**, 447–462, doi:10.1002/qj.49710644905.

Gonzalez, P. L. M., L. Goddard, and A. M. Greene, 2013: Twentieth-century summer precipitation in south eastern South America: Comparison of gridded and station data. *Int. J. Climatol.*, **33**, 2923–2928, doi:10.1002/joc.3633.

——, L. M. Polvani, R. Seager, and G. J. P. Correa, 2014: Stratospheric ozone depletion: A key driver of recent precipitation trends in south eastern South America. *Climate Dyn.*, **42**, 1775–1792, doi:10.1007/s00382-013-1777-x.

Harris, I., P. D. Jones, T. J. Osborn, and D. H. Lister, 2014: Updated high-resolution grids of monthly climatic observations—The CRU TS3.10 dataset. *Int. J. Climatol.*, **34**, 623–642, doi:10.1002/joc.3711.

Huang, H.-P., R. Seager, and Y. Kushnir, 2005: The 1976/77 transition in precipitation over the Americas and the influence of tropical sea surface temperature. *Climate Dyn.*, **24**, 721–740, doi:10.1007/s00382-005-0015-6.

Jia, L., and Coauthors, 2015: Improved seasonal prediction of temperature and precipitation over land in a high-resolution GFDL climate model. *J. Climate*, **28**, 2044–2062, doi:10.1175/JCLI-D-14-00112.1.

Jones, C., and L. M. V. Carvalho, 2013: Climate change in the South American monsoon system: Present climate and CMIP5 projections. *J. Climate*, **26**, 6660–6678, doi:10.1175/JCLI-D-12-00412.1.

Kang, S. M., L. M. Polvani, J. C. Fyfe, and M. Sigmond, 2011: Impact of polar ozone depletion on subtropical precipitation. *Science*, **332**, 951–954, doi:10.1126/science.1202131.

Kushner, P. J., I. M. Held, and T. L. Delworth, 2001: Southern Hemisphere atmospheric circulation response to global warming. *J. Climate*, **14**, 2238–2249, doi:10.1175/1520-0442(2001)014<0001:SHACRT>2.0.CO;2.

Lu, J., G. A. Vecchi, and T. Reichler, 2007: Expansion of the Hadley cell under global warming. *Geophys. Res. Lett.*, **34**, L06805, doi:10.1029/2006GL028443.

Meinshausen, M., and Coauthors, 2011: The RCP greenhouse gas concentrations and their extension from 1765 to 2300. *Climatic Change*, **109**, 213, doi:10.1007/s10584-011-0156-z.

Polvani, L. M., D. W. Waugh, G. J. P. Correa, and S.-W. Son, 2011: Stratospheric ozone depletion: The main driver of twentieth-century atmospheric circulation changes in the Southern Hemisphere. *J. Climate*, **24**, 795–812, doi:10.1175/2010JCLI3772.1.

Robertson, A. W., and C. R. Mechoso, 1998: Interannual and decadal cycles in river flows of southeastern South America. *J. Climate*, **11**, 2570–2581, doi:10.1175/1520-0442(1998)011<2570:IADCIR>2.0.CO;2.

Schneider, U., A. Becker, P. Finger, A. Meyer-Christoffer, B. Rudolf, and M. Ziese, 2011: GPCC full data reanalysis at 0.5°: Monthly land-surface precipitation from rain-gauges built on GTS-based and historic data, version 6.0. Deutscher Wetterdienst/Global Precipitation Climatology Centre, accessed 20 August 2015, doi:10.5676/DWD_GPCC/FD_M_V6_050.

Seager, R., and Coauthors, 2007: Model projections of an imminent transition to a more arid climate in southwestern North America. *Science*, **316**, 1181–1184, doi:10.1126/science.1139601.

——, N. Naik, W. Baethgen, A. Robertson, Y. Kushnir, J. Nakamura, and S. Jurburg, 2010: Tropical oceanic causes of interannual to multidecadal precipitation variability in southeast South America over the past century. *J. Climate*, **23**, 5517–5539, doi:10.1175/2010JCLI3578.1.

Taylor, K. E., R. J. Stouffer, and G. A. Meehl, 2012: An overview of CMIP5 and the experiment design. *Bull. Amer. Meteor. Soc.*, **93**, 485–498, doi:10.1175/BAMS-D-11-00094.1.

Vecchi, G. A., and B. J. Soden, 2007: Global warming and the weakening of the tropical circulation. *J. Climate*, **20**, 4316–4340, doi:10.1175/JCLI4258.1.

——, ——, A. T. Wittenberg, I. M. Held, A. Leetmaa, and M. J. Harrison, 2006: Weakening of tropical Pacific atmospheric circulation due to anthropogenic forcing. *Nature*, **441**, 73–76, doi:10.1038/nature04744.

——, and Coauthors, 2014: On the seasonal forecasting of regional tropical cyclone activity. *J. Climate*, **27**, 7994–8016, doi:10.1175/JCLI-D-14-00158.1.

Viglizzo, E. F., and F. C. Frank, 2006: Ecological interactions, feedbacks, thresholds and collapses in the Argentine Pampas in response to climate and farming during the last century. *Quat. Int.*, **158**, 122–126, doi:10.1016/j.quaint.2006.05.022.

Walker, C. C., and T. Schneider, 2006: Eddy influences on Hadley circulations: Simulations with an idealized GCM. *J. Atmos. Sci.*, **63**, 3333–3350, doi:10.1175/JAS3821.1.

Wu, Y., R. Seager, M. Ting, N. Naik, and T. A. Shaw, 2012: Atmospheric circulation response to an instantaneous doubling of carbon dioxide. Part I: Model experiments and transient thermal response in the troposphere. *J. Climate*, **25**, 2862–2879, doi:10.1175/JCLI-D-11-00284.1.

——, ——, T. A. Shaw, M. Ting, and N. Naik, 2013: Atmospheric circulation response to an instantaneous doubling of carbon dioxide. Part II: Atmospheric transient adjustment and its dynamics. *J. Climate*, **26**, 918–935, doi:10.1175/JCLI-D-12-00104.1.

Yang, X., G. A. Vecchi, T. L. Delworth, K. Paffendorf, R. Gudgel, L. Jia, S. D. Underwood, and F. Zeng, 2015: Extreme North America winter storm season of 2013/14: Roles of radiative forcing and the global warming hiatus. *Bull. Amer. Meteor. Soc.*, **96** (Suppl.), S25–S28, doi:10.1175/BAMS-D-15-00133.1.

Yin, J. H., 2005: A consistent poleward shift of the storm tracks in simulations of 21st century climate. *Geophys. Res. Lett.*, **32**, L18701, doi:10.1029/2005GL023684.